mathematics

MDPI

Article

Rapid Estimation of Contact Stresses in Imageless Total Knee Arthroplasty

Jun Young Kim [1], Muhammad Sohail [1] and Heung Soo Kim [2,*]

[1] Department of Mechanical Engineering, Dongguk University-Seoul, 30 Pildong-ro 1gil, Jung-gu, Seoul 04620, Republic of Korea; jykim_446@dgu.ac.kr (J.Y.K.); sohail@dgu.ac.kr (M.S.)
[2] Department of Mechanical, Robotics and Energy Engineering, Dongguk University-Seoul, 30 Pildong-ro 1-gil, Jung-gu, Seoul 04620, Republic of Korea
* Correspondence: heungsoo@dgu.edu

Abstract: Total knee arthroplasty (TKA) is a surgical technique to replace damaged knee joints with artificial implants. Recently, the imageless TKA has brought a revolutionary improvement to the accuracy of implant placement and ease of surgical process. Based on key anatomical points on the knee, the software guides the surgeon during the TKA procedure. However, the number of revision surgeries is increasing due to malalignment caused by registration error, resulting in imbalanced contact stresses that lead to failure of the TKA. Conventional stress analysis methods involve time-consuming and computationally demanding finite element analysis (FEA). In this work, a machine-learning-based approach estimates the contact pressure on the TKA implants. The machine learning regression model has been trained using FEA data. The optimal preprocessing technique was confirmed by the data without preprocessing, data divided by model size, and data divided by model size and optimal angle. Extreme gradient boosting, random forest, and extra trees regression models were trained to determine the optimal approach. The proposed method estimates the contact stress instantly within 10 percent of the maximum error. This has resulted in a significant reduction in computational costs. The efficiency and reliability of the proposed work have been validated against the published literature.

Keywords: imageless navigator; total knee arthroplasty; finite element analysis; machine learning

MSC: 92C50

Citation: Kim, J.Y.; Sohail, M.; Kim, H.S. Rapid Estimation of Contact Stresses in Imageless Total Knee Arthroplasty. *Mathematics* **2023**, *11*, 3527. https://doi.org/10.3390/math11163527

Academic Editors: Maria Hadjinicolaou and Foteini Kariotou

Received: 4 July 2023
Revised: 9 August 2023
Accepted: 13 August 2023
Published: 15 August 2023

1. Introduction

Total knee arthroplasty (TKA) is a surgical procedure to replace damaged knee joints with artificial implants. The procedure has proven exceptional performance in reducing pain and enhancing the life quality of the patients through deformity correction and restoration of the motion range in the lower extremities [1]. The traditional TKA that is performed relies on surgeon skills and mechanical equipment, such as mechanical tensors and templates [2]. For a more accurate procedure, the computer-assisted or imageless TKA technique has been developed, which yields greater correction of the alignment of lower extremities by capturing the locations of the anatomical points and calculating their alignment status in real-time [3,4]. With the development of the imageless technique, the risk of transfusion and side effects are lessened without increasing cost while reducing the overall surgical time [5]. Although TKA became more precise using the imageless technique, the number of revision surgeries is increasing due to various reasons. Kurtz et al. projected that revision surgeries of TKA will increase by 600 percent by 2030 [6]. Schorer et al. reported that among 844 patients who underwent revision TKA, 10 percent of patients suffered from polyethylene wear, while 6.6 percent of patients suffered from malalignment [7]. According to the statistics from 1979 to 2009, 8.2 percent of patients underwent revision surgery due to component wear [8]. Malalignment can occur due to

errors during bone cuts and registration in imageless TKA [9,10]. Davis et al. reported that a 6.5 mm registration error of the distal femoral center caused an error of 5.2° valgus in the femoral mechanical axis [11]. If the degree of malalignment increases, the greater the force and contact stress that will be applied to the implants, which will be biased to one side [12]. Increased contact stress on implants is the main reason for cold flow and wear in TKA [13]. Hence, to reduce the frequency of revision surgery, it is essential to monitor the degree of contact stress applied to the implant.

Most of the methods for analyzing the degree of contact stress due to malalignment involve finite element analysis (FEA) [14–17]. By using FEA, it is possible to determine the value and position of the maximum contact stress by considering the patient's weight, alignment status, and implant size [18]. Suh et al. analyzed the knee joints using FEA and confirmed that the varus alignment status would increase the value of contact stress [17]. Gheorghiu et al. proposed the FEA method for the estimation of cemented knee implants in TKA, correlating the clinical outcomes of the procedure [19]. Woiczinski et al. conducted FEA on the weight-bearing TKA model and investigated the clinical aspect of TKA using the unresurfaced patella [20]. Lee et al. assessed the stress of the patella surface after and before surgery and correlated it with anterior knee pain [21]. However, FEA can only produce results for one patient at a time since the size of the implant and the load applied to it differ for each patient [22].

Recently, the emerging data-driven approaches with machine learning techniques have been adapted to the medical field due to their exceptional capabilities in identification and prediction [20–22]. Conventional machine learning techniques, such as extreme gradient boosting (XGB), random forest (RF), and support vector machine (SVM), have been widely used to estimate clinical results [23–25]. Machine learning is used in the medical field in several ways, for example, in cancer prediction, mortality prediction, decision-making, and diagnosis [25–28]. Also, the extra trees (ET) algorithm is attracting attention in the medical field due to its strength in random data [29]. The ET algorithm has a similar structure to the RF algorithm, but the sampling method is totally random, which creates trees with unique samples [29]. The working principles of algorithms are shown in Table 1. It has outperformed RF in brain tumor segmentation and is used in various fields, such as smart buildings and malware detection, proving its performance [30–32]. Several cases have adapted machine learning to orthopedics. Merali et al. adapted the RF model to estimate the outcome of degenerative cervical myelopathy surgery [24]. Jun et al. proposed a contact stress prediction method on total hip replacement implants using principal component analysis and SVM [33]. Kruse et al. reported that the XGB algorithm is capable of predicting hip fractures [34]. However, no study has estimated contact stress in TKA using machine learning techniques.

Table 1. The working principles of algorithms.

Algorithm	Working Principle
XGB	Ensemble of decision trees; loss function of second-order Taylor expansion [35].
RF	Ensemble of decision trees; increased diversity of the trees through the bagging procedure [36].
SVM	Predicts a continuous output while maximizing the margin between the classes [37].
ET	Ensemble of decision trees; a more randomized sampling method compared to RF [29].

Motivated by the limitations, this work presents a robust and rapid contact stress estimation technique using Latin hypercube sampling (LHS) and the machine learning regression model. To create a robust model, a large number of input values, such as weight, alignment status, and more, are sampled through LHS because it provides good

distribution characteristics and high computation efficiency [38,39]. LHS is an advanced approach to Monte Carlo simulation, which divides the range of input variables to have the same intervals and samples value from it. Also, the enhanced stochastic evolutionary (ESE) algorithm, which is used for LHS, shows great power when producing space-filling designs for multivariate situations [40]. The output values, maximum contact stresses, are created through FEA using the sampling input values. The optimal alignment status in each model is determined by utilizing the minimum contact stress from maximum varus angle to maximum valgus angle under 100 kg load for a single knee joint. Then, the total dataset is divided into three categories depending on what preprocessing was applied: no preprocessing, divided by each size, and divided by each optimal alignment status, to determine which preprocessing is the best method. For regressors, XGB, RF, and ET were chosen for their excellent predictive performance and speed. The machine learning regressors were trained with 70 percent of randomly divided data. The remaining 30 percent of untrained data or test data were compared with the estimated contact stress values from trained models, and each preprocessing type and model were compared using metrics, such as the mean squared error (MSE) and mean absolute error (MAE). With the best preprocessing type and model, the contact stress value from the maximum varus angle to the maximum valgus angle under 100 kg loading was predicted to compare with the FEA value. The rest of this paper is structured as follows: Section 2 describes the CAD, FEA, and prediction model development. Section 3 compares the prediction results from each model, showing the accuracy of the best prediction model and the advantage of using a machine-learning-based approach instead of traditional FEA results. Finally, Section 4 presents the conclusions and provides future perspectives.

2. Methodology

2.1. TKA Procedure

The surgical techniques for imageless TKA used here follow the method of Schwarzkopf et al. [41]. The surgical device consists of a pair of cameras, optical trackers, and a computer station that can save the location of anatomical landmarks and calculate the information for the surgeon. Figure 1a shows the anatomical landmark acquisition part, or registration process and locations.

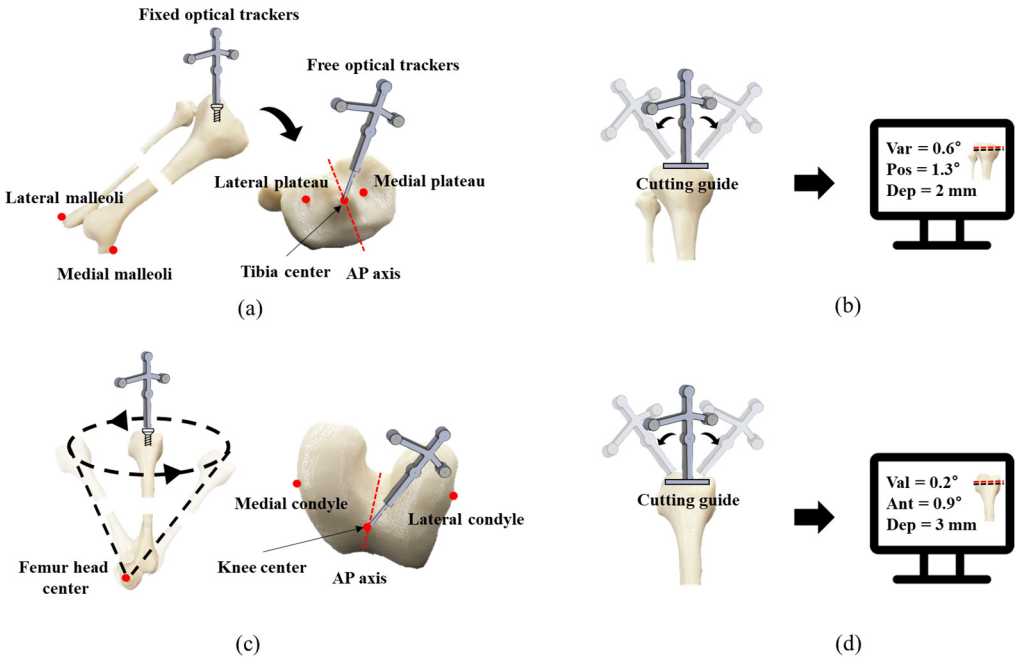

Figure 1. (**a**) Registration process of tibia, (**b**) calculation and resection process of tibia, (**c**) registration process of femur, and (**d**) calculation and resection process of femur.

After the surgeon performs the incision and exposure of the lower extremities, a bone screw with optical trackers, or fixed optical trackers, is drilled into the tibia. The anatomical landmarks are registered with free optical trackers. The location of the tibial center, the medial and lateral malleoli, the anteroposterior (AP) axis, and the medial and lateral plateaus are registered. Then, the cutting guide is attached to the bottom of the tracker, where the computer station provides the real-time calculation of cut measurements, as shown in Figure 1b. The position of the cutting guide is moved to the optimal point and then fixed with pins to stop further movement, and bone resection is performed. Figure 1c shows the location of landmarks and the process for the femur. The surgical step for the femur is similar to that of the tibia. After the optical tracker is attached to the femur, the rotation is given to capture the center of rotation, which will be registered as the femur head center. The AP line for the femur, the knee center (KC), and the lateral and medial femoral condyles are registered in the same way as the tibia. The same as the tibial part that is illustrated, the cutting guide is fixed to the femur after the femoral registration and bone resection are performed, as shown in Figure 1d.

Based on the registered anatomical points, the TKA system software constructs the virtual femoral and tibial coordinate system. For this study, the methodology developed in a previous study was used [42], where the femoral coordinate system (FCS) was assigned using the femoral mechanical axis and anatomical transepicondylar axes. The AP axis at the distal femur was defined using the cross product. Similarly, the tibial coordinate system (TCS) was assigned using the tibial mechanical and anteroposterior axes. The tibial third axis was determined according to the right-hand rule.

2.2. CAD Model Development

To develop the FEM model, CAD model creation and boundary conditions were carried out in commercial CAD software (Solidworks, Dassault Systems, Vellizy-Villacoublay, France). Figure 2 shows the assembled model of the femoral component and plastic spacer with different sizes that were designed using the parameters of the existing model (Exult Knee System, Corentec, Seoul, Republic of Korea) in Solidworks.

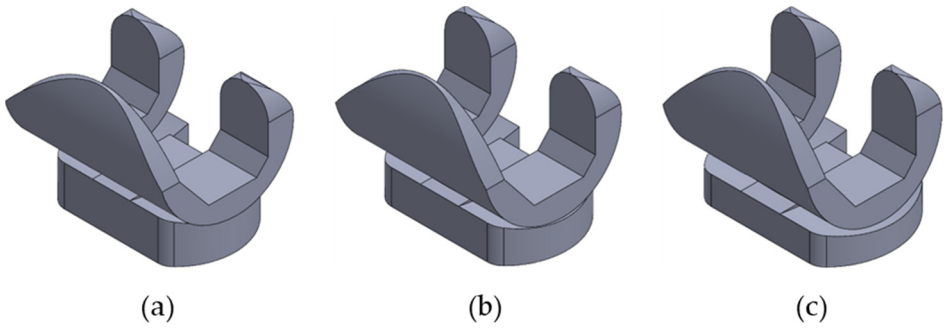

Figure 2. (**a**) F1/T2 assembled model, (**b**) F7/T6 assembled model, and (**c**) F13/T11 assembled model.

Due to privacy restrictions imposed by Corentec, certain parameters such as curvature of articulating surface and ratio of medial and lateral parts were not provided and thus had to be estimated. Although there are posterior-stabilized types and cruciate-retaining types of implants, in this study, only the cruciate-retaining type is considered. The sizing of implants in the femur and tibia is calculated based on the mediolateral (ML) and AP length of the bone [43]. There are 13 types of femur components and 10 types of plastic spacers considering the ML and AP length, and there are compatible combinations. The femoral component of size 1 is named F1. Similarly, the plastic spacer of size 2 is named T2. Among them, the smallest, medium, and largest combinations were selected to compare the prediction accuracy by size. In the smallest combination, the femoral component, the F1 model, had an AP length of 59 mm and an ML length of 50 mm, while the plastic spacer, the T2 model, had an AP length of 36 mm and an ML length of 57 mm. Table 2 lists the ML and AP length of the medium combination, F7/T6, and the largest combination, F13/T11.

Table 2. AP and ML length of each combination.

Set	F1/T2	F7/T6	F13/T11
AP length (mm)	50/36	62/44	76/57
ML length (mm)	59/57	67/69	78/86

The femoral component and plastic spacer were aligned such that the femoral and tibial mechanical, lateromedial, and anteroposterior axes were parallel to each other; moreover, the femoral component and plastic spacer had a contact condition. As contact stress reaches the maximum at 100% of the deep knee bend cycle [44], to obtain the maximum value, the femoral component and plastic spacer were aligned when the deep knee bend cycle was at 100 percent.

2.3. FEA Model Development

Based on the 3D CAD model, the FEA model was created. The assembled model of the femoral component and plastic spacer was imported into FEA software. For comparison with the reference, all the conditions were set the same as the reference [18].

The contact surface between the femoral component and the plastic spacer was modeled as continuous bonds. A tangential contact condition was applied between two implants, and the coefficient of friction was assumed to be 0.07 [45,46].

The femoral component was made of titanium alloy (Ti6Al4V). The plastic spacer was made of ultra-high molecular weight polyethylene (UHMWPE), which is widely used in the field of orthopedics for its biocompatibility, chemical resistance, and wear resistance [47]. Moreover, the Ti6Al4V and UHMWPE were assumed to be homogeneous and isotropic [18,48–50](Table 3).

Table 3. Material properties of the FE model.

	Young's Modulus (MPa)	Poisson's Ratio
Ti6Al4V alloy	110,000	0.30
UHMWPE	685	0.47

The femoral component and plastic spacer were modeled using a ten-noded 3D quadratic tetrahedron (C3D10). Table 4 shows the detailed number of elements in each implant. For model validation, the number of meshes was set as similar to Kang et al. [18]. For the femoral components and plastic spaces, the mesh sizes were set to 2.3 and 2.7, respectively. Between the F1 model and F7 model, the increment of the number of elements showed the largest due to the increase in the size of the model.

Table 4. Number of elements used for different sizes of implants.

Set	F1/T2	F7/T6	F13/T11
Femoral component	15,909	29,866	34,347
Plastic spacer	9448	13,529	23,598
Total	25,357	43,395	57,945

The assembled TKA model with femoral component and plastic spacer has six degrees of freedom. Kang et al. applied four types of loading conditions [18]. First, 150 N of force was applied to the tibia to measure anterior–posterior translation. For the second loading condition, 1150 N of axial loading was applied to calculate the contact pressure on plastic spacers. For the third loading condition, 50 N of conservative ankle force and hamstring forces concerning flexion angle were applied. The last loading condition was applied for the deep knee bend cycle. In this paper, contact stress is the only interest, and the magnitude of the force from the other loading conditions is minor, with the loading conditions, except for the second, being ignored.

The force distribution on the medial and lateral sides differs due to alignment status. Werner et al. investigated the force distribution of each side of the compartments according to the alignment state [51]. At neutral alignment, 57 percent of the force was distributed on the medial side. As the alignment status went to a valgus state, the force on the medial side increased. At 5° valgus, 91 percent of the force was distributed at the medial side. The force distribution on the other side increased as the alignment status went to the varus state, showing 79 percent on the lateral side. Figure 3 shows the medial and lateral force distribution due to the varus/valgus angle [51]. The force distribution on each side is normalized and fitted using linear regression. The fitted equations for the distribution rate of each side are as follows:

$$P_L = 0.0925\alpha + 0.4843 \quad (1)$$

$$P_M = 1 - P_L \quad (2)$$

where α is the alignment status. For imageless-based TKA, the maximum range of error is from 5° valgus to 3° varus [11]. The range of α is set as the same.

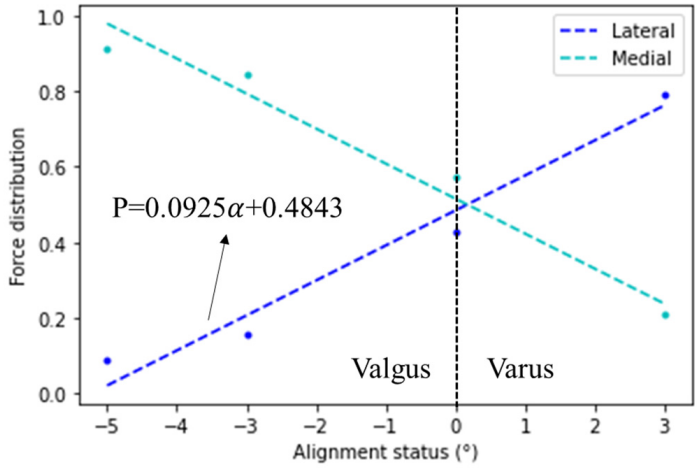

Figure 3. Force distribution due to alignment status.

For validation, the contact stresses have been obtained from the literature. At neutral alignment, a force of 1150 N is provided as compressive force, along with the femoral mechanical axis, and the variations in contact stress due to the weight of the patient have been investigated by using a range of patient weight of (30 to 100) kg [18]. The maximum load on one side of the implant can be three times the weight of the patient; the equations for converting weight to load are as follows [52]:

$$F_L = 3gP_LW \quad (3)$$

$$F_M = 3gP_MW \quad (4)$$

where F_L is the load applied to the lateral side, F_M is the load applied to the medial side, g is gravitational acceleration, and W is the patient's weight in kg. In the calculation, the varus status was assigned a positive value, whereas the valgus status was assigned a negative value. To apply different loads to the medial and lateral sides, the femoral component is divided into two halves about the femoral AP axis.

Figure 4 shows the boundary conditions applied in this study. For the femoral component, internal–external rotation, varus–valgus rotation, and translation in the AP axis direction were fixed. For the plastic spacer, flexion–extension rotation, medial–lateral translation, and translation in the AP axis direction were fixed. The remaining boundary conditions were set free [18].

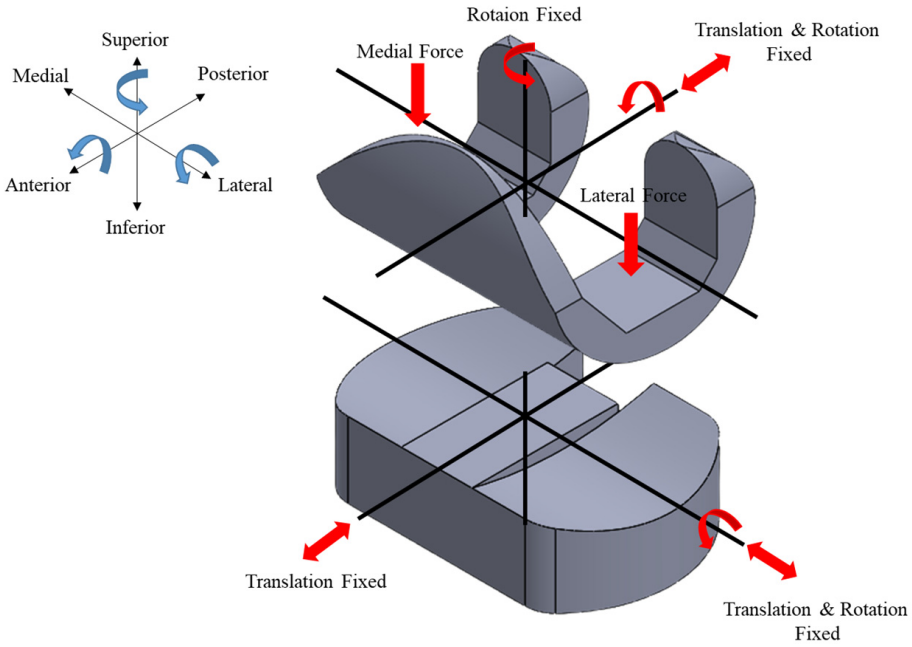

Figure 4. Loading and boundary conditions for the TKA implant.

2.4. Prediction Model Development

In this section, the development of the contact stress estimation model is demonstrated. Figure 5 shows the total process of contact stress prediction. To create the maximum contact stress prediction model, training data for each variable must first be generated. Input variables were generated using LHS, and output data were created using the developed FEM model in the previous section. To determine the best preprocessing and algorithm, multiple methods were applied and compared.

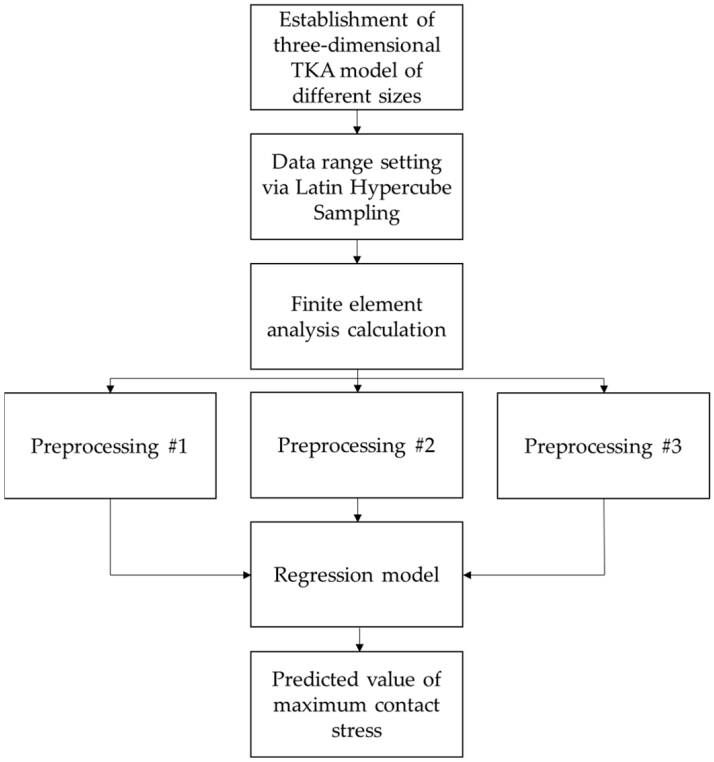

Figure 5. Prediction process of contact stress on plastic spacer.

In this study, the alignment status and weight of the patients are sampled using LHS for (3° varus to 5° valgus) and (30 to 100) kg weight. According to the sampled alignment status and weight, the forces applied to each side were calculated using Equations (3) and (4). With 180 samples per model, a total of 540 samples were generated. Figure 6 shows the generated samples of each implant model. Different sizes of the TKA model were analyzed using the ABAQUS software (Simulia, Providence, RI, USA). Contact force on the plastic spacer was investigated with respect to different sizes, sampled weight, and alignment status.

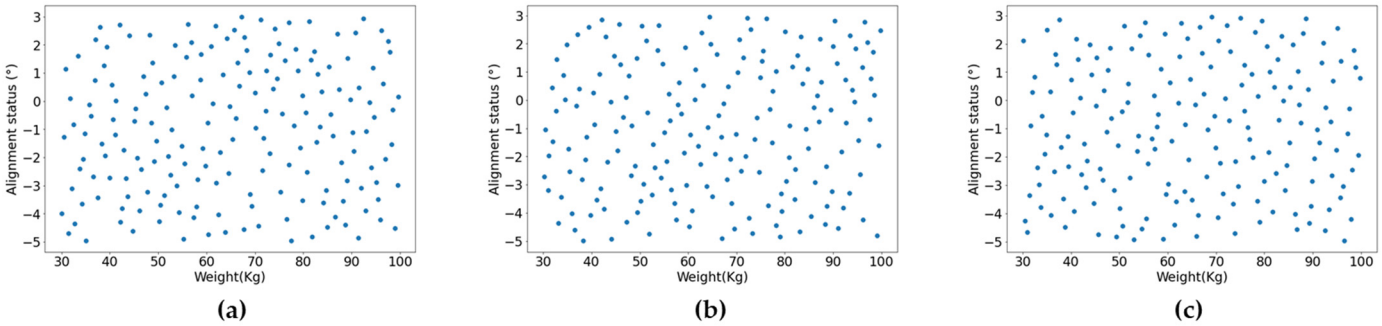

Figure 6. Sampled alignment status and weight of the (**a**) F1/T2, (**b**) F7/T6, and (**c**) F13/T11 models.

Before data preprocessing, finite element calculation was performed for each model under the 100 kg loading condition and varying alignment status to determine which alignment status was optimum for the model. For the F1/T2 model, a 0.6° varus angle resulted in minimum contact stress of 25.5 MPa. For the F7/T6 model, a 0.5° varus angle resulted in minimum contact stress of 21.64 MPa. The optimal value of the third model, F13/T11, was found at a 1° valgus angle with a contact stress of 18.42 MPa. The results under the 100 kg loading condition are shown in Figure 7.

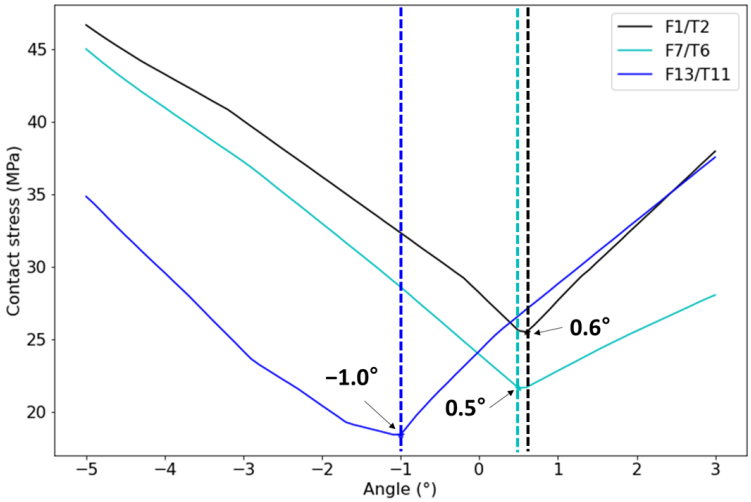

Figure 7. Finite element calculation result of each model under the 100 kg loading condition.

The impact of data preprocessing on the results was evaluated by the implementation of three different techniques on the dataset. Figure 8 shows the three different preprocessing types. Figure 8a shows the first data, which is the raw data from the FEA result without any preprocessing. Figure 8b shows the second data, which is divided into three parts for each model: F1/T2, F7/T6, and F13/T11. Figure 8c shows the third data, which is obtained by dividing the data for each model based on the optimal alignment status. After dividing the data, each data was normalized using MinMaxScaler.

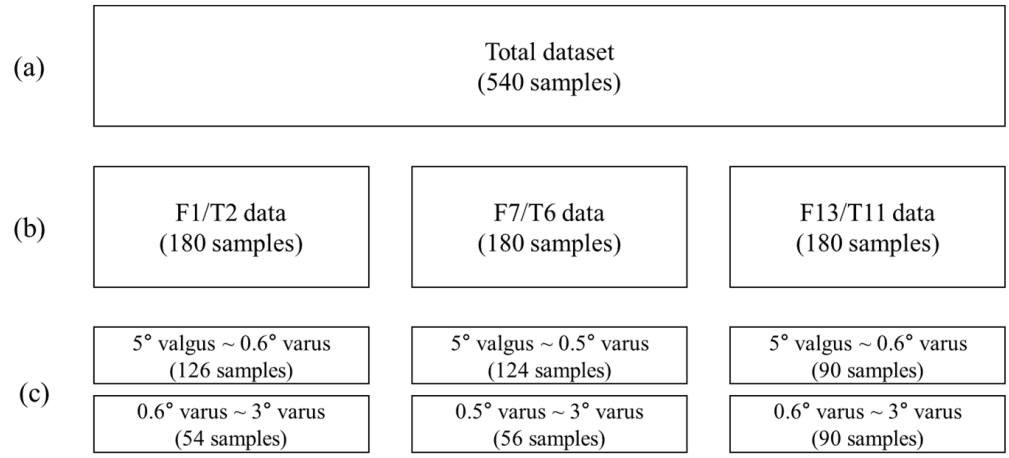

Figure 8. (**a**) Dataset with no preprocessing. (**b**) Dataset divided by each size. (**c**) Dataset divided by each optimal alignment status.

Each preprocess dataset is divided into 70% training data and 30% test data. The training data is used to train XGB, RF, and ET regressors, and the test data are compared with the estimated values from the trained regression model using the evaluation criteria. For the evaluation criteria, r^2, mean absolute error (MAE), mean squared error (MSE), maximum error, and maximum percentage error were used and are represented by Equations (5)–(9) [53,54]:

$$r^2 = \left(\frac{\sum_{i=1}^{n} (y - \overline{y})^2 (\hat{y} - \overline{\hat{y}})^2}{\sqrt{\sum_{i=1}^{n} (y - \overline{y})^2} \sqrt{\sum_{i=1}^{n} (\hat{y} - \overline{\hat{y}})^2}} \right) \tag{5}$$

$$MAE = \frac{1}{N} \sum_{i=1}^{N} |y_i - \hat{y}_1| \tag{6}$$

$$MSE = \frac{1}{N} \sum_{i=1}^{N} (y_i - \hat{y}_1)^2 \tag{7}$$

$$Maximum\ error = \max(|y - \hat{y}|) \tag{8}$$

$$Maximum\ percentag\ eerror = \max\left(\frac{y - \hat{y}}{y} \right) \times 100 \tag{9}$$

where y_i is the actual contact stress from the FEA model, $\overline{y}$ is the average value of y_i, $\hat{y}$ is the predicted contact stress estimated by the regression model, and N is the total number of samples.

3. Results and Discussion

3.1. Validation of FEM Model

The maximum contact stress value is compared with the reference to validate the developed CAD and FEA models [18]. In the loading condition of 1150 N with neutral alignment status and at 100% of the deep knee bend cycle, Kang et al. reported 15 MPa of contact stress at the plastic spacer [18]. In the TKA model, the F1/T2 model showed 14.07 MPa. Figure 9 shows the FEA result of the F1/T2 model. This minor difference could be caused by differences in the model size and geometry. However, this result indicates good agreement between the model used in this study and the existing model.

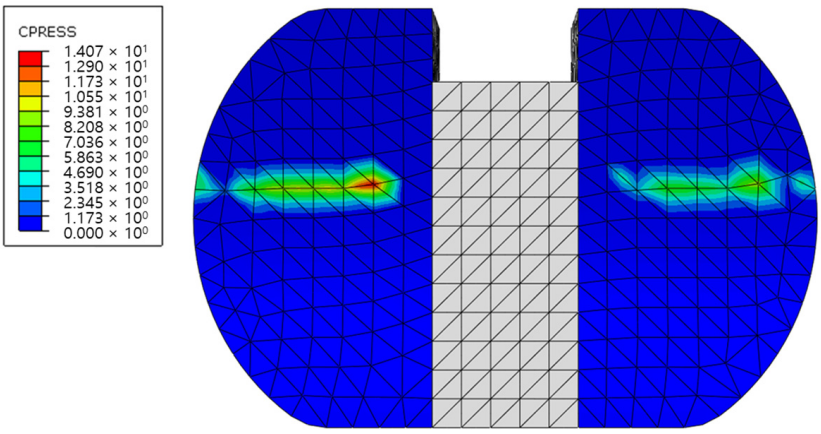

Figure 9. Stress distribution in the plastic spacer.

3.2. Results of Data Generation

Figure 10 shows the finite element calculation for each model. For the F1/T2 model, the maximum contact pressure of 44.64 MPa was calculated at a 4.51° valgus angle. The minimum value was calculated as 11.48 MPa at 1.14° varus and 30.92 kg weight. For the F7/T6 model, the maximum value of 43.81 MPa showed the alignment status of 4.8° valgus and 99.1 kg weight. The minimum value of 8.106 MPa was observed at 1.44° varus and 32.7 kg applied weight. For F13/T11, the largest model, the maximum value of 34.23 MPa was observed at the alignment status of 2.55° varus at 95.08 kg weight. The minimum value of 6.024 MPa occurred at 0.9° valgus and 31.61 kg weight.

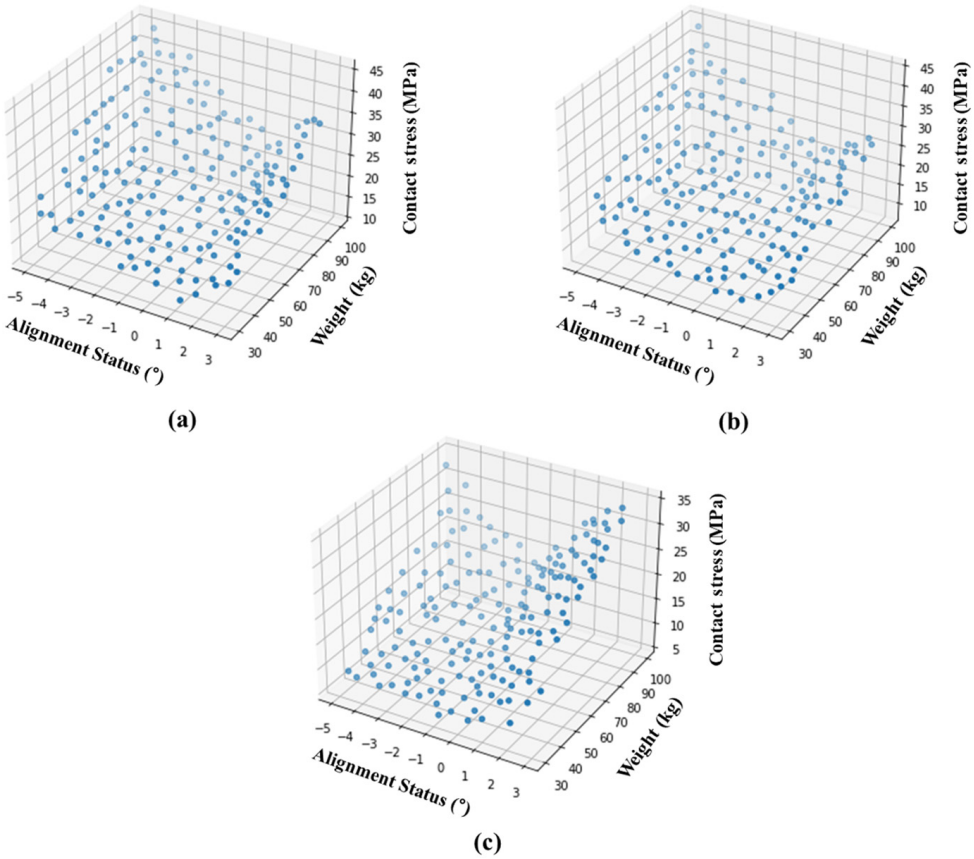

Figure 10. Results of FEA for the (**a**) F1/T2, (**b**) F7/T6, and (**c**) F13/T11 models.

As the alignment status moved away from the optimum angle, the amount of contact stress increased; moreover, in the case of high weight, the increment was significant. For the F1/T2 and F7/T6 models, the maximum contact stress occurred around 5° valgus, which is the lower boundary of sampling. For the F13/T11 model, the maximum contact stress occurred around 3° varus, which is the upper boundary.

3.3. Results of Contact Stress Prediction

Figure 11 shows the metrics obtained from each model and preprocessing. If the metrics are from the XGB regressor trained by the first preprocessed data, it is labeled as XGB1, and the same is applied to the other metrics. It is confirmed that the third preprocessing will increase the model performance, showing superior results in all three models. The change in metrics according to the type of preprocessing was most noticeable in the case of RF regressors. RF3 showed 13.36 percent of maximum percentage error, which is 17.62 percent lower than RF1, and 7.87 percent lower than RF2. Also, 0.83 MPa of MAE decreased when the third preprocessing data was used instead of the first preprocessed data. Other models showed similar behavior, improving the metrics.

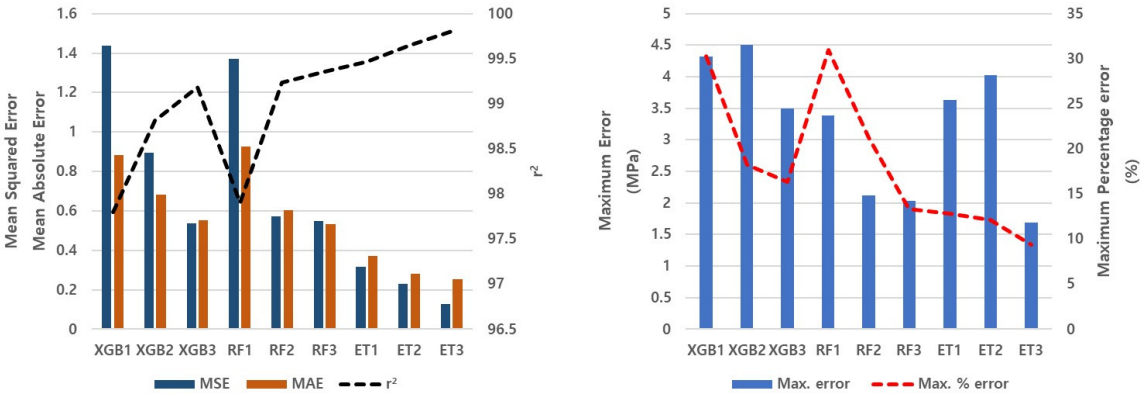

Figure 11. Metrics according to each model and preprocessing type.

A comparison between the models revealed that the ET regressor was the best model. It was most prominent when the first preprocessed data was used. The ET1 showed superior results to the other models trained with the first preprocessed data in all metrics. It showed 12.82 percent of the maximum percentage error when XGB1 was 30.31 percent and RF1 was 30.98 percent. Among all the models, the ET3 model, which is the ET regressor model trained using the third preprocessed data, showed the best performance. It showed 9.398 percent of maximum percentage error and 1.689 MPa of maximum error. Table 5 shows the metrics for the ET3 model. The metrics reveal that the ET regressor trained with the proposed preprocessing can estimate a reliable maximum contact stress value for any size, weight, or alignment state.

Table 5. The metrics of ET3 model.

MAE	MSE	r^2 (%)	Max. Error (MPa)	Max. % Error (%)
0.1281	0.2536	99.80	1.689	9.398

To verify the ET3 model, the contact stress value was predicted with the input of the data used in Figure 7, and the actual value derived through FEA was compared. Figure 12 shows the result of contact stress prediction under 100 kg loading in different sizes using the ET3 model. Overall, the predicted contact stress value followed the behavior of the actual contact stress well. It was shown that the prediction performance was less accurate in the boundary area. Nevertheless, the ET3 model estimated a value within the error range.

In this case, the maximum error occurred at the prediction of the F13/T11 model's 3° varus case, showing a value of 3.598 MPa, and an error of 9.581 percent. In the 3° varus status, the F1/T2 and F7/T6 models showed the maximum errors of (3.124 and 1.387) MPa, and percentage errors of (8.229 and 4.945) percent, respectively. Through this, it was confirmed that the ET regressor with the proposed preprocessing can robustly predict the unlearned data as well. By using the proposed method, the contact stress occurring on the joint of the patient can be immediately estimated. Through this, it becomes possible for the surgeon to evaluate the results of the surgery just by entering the information of the patient, such as weight and alignment status, which allows the surgeon to check the need for revision surgery and guide the patient.

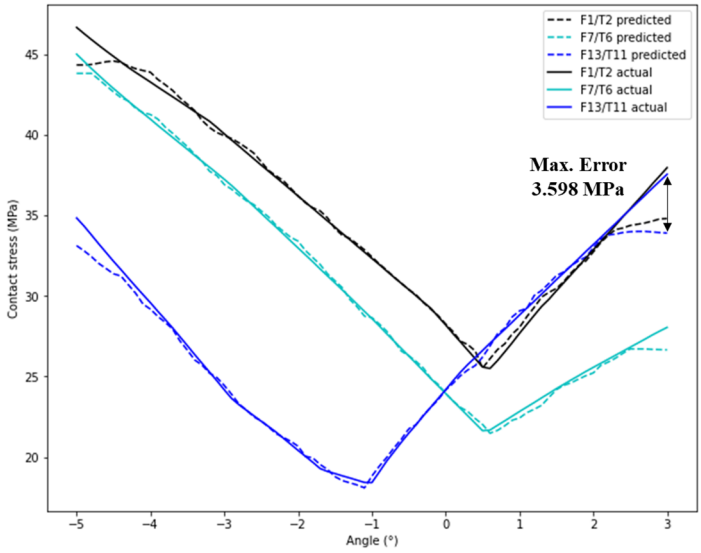

Figure 12. Results of contact stress prediction using the ET3 model.

4. Conclusions

It is necessary to analyze the degree of contact stress applied to the implant to reduce the frequency of revision surgeries in TKA. The conventional method, which involves FEA, can provide a wide range of information. However, computation time and resources limit its practical application. In this work, a machine-learning-based approach is proposed that estimates the maximum contact stress to determine the success of TKA surgery. This technique requires a large amount of contact stress data for various weights, sizes, and alignment statuses. The input generated through LHS was calculated using FEA to derive the contact stress value. The validity of data was validated against a benchmark study. Three different data subsets were created: the data with no preprocessing, the data divided concerning the size of the model, and the data divided according to the size and optimal angle of the model were created and trained using XGB, RF, and ET regressors. It was confirmed that the ET regressor trained with data divided according to size and optimal angle could estimate the maximum contact stress within 10 percent of the error, regardless of the weight, implant size, and alignment status. In addition, after the model is trained, the value can be estimated immediately without a separate calculation time, which can be used during the consultation time between the surgeon and the patient. However, there are limitations in the proposed method since certain parameters, such as ligament, or osteoarthritis grade, were not considered. For future studies, data considering the stages of the bone disease will be generated and added as an input variable.

Author Contributions: Conceptualization, J.Y.K. and H.S.K.; methodology, J.Y.K. and H.S.K.; software, J.Y.K.; validation, J.Y.K.; writing—original draft preparation, J.Y.K. and M.S.; writing—review and editing, H.S.K.; supervision, H.S.K.; project administration, H.S.K.; funding acquisition, H.S.K. All authors have read and agreed to the published version of the manuscript.

Funding: This work was supported by the Ministry of Trade, Industry, and Energy (MOTIE) and the Korea Institute for Advancement of Technology (KIAT) through the International Cooperative R&D program (Project No. P0016173) and also supported by the MOTIE (Ministry of Trade, Industry, and Energy) in Korea, under the Fostering Global Talents for Innovative Growth Program (P0017307) supervised by the Korea Institute for Advancement of Technology (KIAT). Special thanks to Professor Aditi Chattopadhyay for revising this work.

Data Availability Statement: Not applicable.

Conflicts of Interest: The authors declare no conflict of interest.

References

1. Rajgopal, A.; Ahuja, N.; Dolai, B. Total Knee Arthroplasty in Stiff and Ankylosed Knees. *J. Arthroplast.* **2005**, *20*, 585–590. [CrossRef]
2. Boulos, A.; Lemme, N. Total Knee Arthroplasty. In *Essential Orthopedic Review*; Springer: Cham, Switzerland, 2018; pp. 165–168. [CrossRef]
3. Bae, D.K.; Song, S.J. Computer Assisted Navigation in Knee Arthroplasty. *Clin. Orthop. Surg.* **2011**, *3*, 259–267. [CrossRef] [PubMed]
4. Stulberg, S.D.; Yaffe, M.A.; Koo, S.S. Computer-Assisted Surgery versus Manual Total Knee Arthroplasty: A Case-Controlled Study. *J. Bone Jt. Surg.* **2006**, *88*, 47–54. [CrossRef]
5. Tabatabaee, R.M.; Rasouli, M.R.; Maltenfort, M.G.; Fuino, R.; Restrepo, C.; Oliashirazi, A. Computer-Assisted Total Knee Arthroplasty: Is There a Difference Between Image-Based and Imageless Techniques? *J. Arthroplast.* **2018**, *33*, 1076–1081. [CrossRef] [PubMed]
6. Kurtz, S.; Ong, K.; Lau, E.; Mowat, F.; Halpern, M. Projections of Primary and Revision Hip and Knee Arthroplasty in the United States from 2005 to 2030. *J. Bone Jt. Surg.* **2007**, *89*, 780–785. [CrossRef]
7. Schroer, W.C.; Berend, K.R.; Lombardi, A.V.; Barnes, C.L.; Bolognesi, M.P.; Berend, M.E.; Ritter, M.A.; Nunley, R.M. Why Are Total Knees Failing Today? Etiology of Total Knee Revision in 2010 and 2011. *J. Arthroplast.* **2013**, *28*, 116–119. [CrossRef]
8. Sadoghi, P.; Liebensteiner, M.; Agreiter, M.; Leithner, A.; Böhler, N.; Labek, G. Revision Surgery after Total Joint Arthroplasty: A Complication-Based Analysis Using Worldwide Arthroplasty Registers. *J. Arthroplast.* **2013**, *28*, 1329–1332. [CrossRef]
9. Mullaji, A.; Kanna, R.; Marawar, S.; Kohli, A.; Sharma, A. Comparison of Limb and Component Alignment Using Computer-Assisted Navigation Versus Image Intensifier-Guided Conventional Total Knee Arthroplasty.A Prospective, Randomized, Single-Surgeon Study of 467 Knees. *J. Arthroplast.* **2007**, *22*, 953–959. [CrossRef]
10. Schmitt, J.; Hauk, C.; Kienapfel, H.; Pfeiffer, M.; Efe, T.; Fuchs-Winkelmann, S.; Heyse, T.J. Navigation of Total Knee Arthroplasty: Rotation of Components and Clinical Results in a Prospectively Randomized Study. *BMC Musculoskelet. Disord.* **2011**, *12*, 16. [CrossRef]
11. Davis, E.T.; Pagkalos, J.; Gallie, P.A.M.; Macgroarty, K.; Waddell, J.P.; Schemitsch, E.H. Defining the Errors in the Registration Process During Imageless Computer Navigation in Total Knee Arthroplasty: A Cadaveric Study. *J. Arthroplast.* **2014**, *29*, 698–701. [CrossRef]
12. D'Lima, D.D.; Patil, S.; Steklov, N.; Slamin, J.E.; Colwell, C.W. Tibial Forces Measured In Vivo after Total Knee Arthroplasty. *J. Arthroplast.* **2006**, *21*, 255–262. [CrossRef] [PubMed]
13. Srivastava, A.; Lee, G.Y.; Steklov, N.; Colwell, C.W.; Ezzet, K.A.; D'Lima, D.D. Effect of Tibial Component Varus on Wear in Total Knee Arthroplasty. *Knee* **2012**, *19*, 560–563. [CrossRef] [PubMed]
14. Catani, F.; Innocenti, B.; Belvedere, C.; Labey, L.; Ensini, A.; Leardini, A. The Mark Coventry Award Articular: Contact Estimation in TKA Using in Vivo Kinematics and Finite Element Analysis. *Clin. Orthop. Relat. Res.* **2010**, *468*, 19–28. [CrossRef]
15. Innocenti, B.; Labey, L.; Kamali, A.; Pascale, W.; Pianigiani, S. Development and Validation of a Wear Model to Predict Polyethylene Wear in a Total Knee Arthroplasty: A Finite Element Analysis. *Lubricants* **2014**, *2*, 193–205. [CrossRef]
16. Arab, A.Z.E.A.; Merdji, A.; Benaissa, A.; Roy, S.; Bachir Bouiadjra, B.A.; Layadi, K.; Ouddane, A.; Mukdadi, O.M. Finite-Element Analysis of a Lateral Femoro-Tibial Impact on the Total Knee Arthroplasty. *Comput. Methods Programs Biomed.* **2020**, *192*, 105446. [CrossRef]
17. Suh, D.S.; Kang, K.T.; Son, J.; Kwon, O.R.; Baek, C.; Koh, Y.G. Computational Study on the Effect of Malalignment of the Tibial Component on the Biomechanics of Total Knee Arthroplasty: A Finite Element Analysis. *Bone Jt. Res.* **2017**, *6*, 623–630. [CrossRef] [PubMed]
18. Kang, K.T.; Son, J.; Kwon, S.K.; Kwon, O.R.; Park, J.H.; Koh, Y.G. Finite Element Analysis for the Biomechanical Effect of Tibial Insert Materials in Total Knee Arthroplasty. *Compos. Struct.* **2018**, *201*, 141–150. [CrossRef]
19. Gheorghiu, N.; Socea, B.; Dimitriu, M.; Bacalbasa, N.; Stan, G.; Orban, H. A Finite Element Analysis for Predicting Outcomes of Cemented Total Knee Arthroplasty. *Exp. Ther. Med.* **2021**, *21*, 267. [CrossRef] [PubMed]
20. Woiczinski, M.; Steinbrück, A.; Weber, P.; Müller, P.E.; Jansson, V.; Schröder, C. Development and Validation of a Weight-Bearing Finite Element Model for Total Knee Replacement. *Comput. Methods Biomech. Biomed. Engin.* **2016**, *19*, 1033–1045. [CrossRef] [PubMed]

21. Lee, Y.S.; Lee, T.Q.; Keyak, J.H. Effect of an UHMWPE Patellar Component on Stress Fields in the Patella: A Finite Element Analysis. *Knee Surg. Sport. Traumatol. Arthrosc.* **2009**, *17*, 71–82. [CrossRef]
22. Miller, M.D.; Thompson, S.R.; Hart, J. *Review of Orthopaedics E-Book*; Elsevier Health Sciences: Amsterdam, The Netherlands, 2012.
23. Díaz-Alcaide, S.; Martínez-Santos, P. Mapping Fecal Pollution in Rural Groundwater Supplies by Means of Artificial Intelligence Classifiers. *J. Hydrol.* **2019**, *577*, 124006. [CrossRef]
24. Merali, Z.G.; Witiw, C.D.; Badhiwala, J.H.; Wilson, J.R.; Fehlings, M.G. Using a Machine Learning Approach to Predict Outcome after Surgery for Degenerative Cervical Myelopathy. *PLoS ONE* **2019**, *14*, e0215133. [CrossRef] [PubMed]
25. Hayward, J.; Alvarez, S.A.; Ruiz, C.; Sullivan, M.; Tseng, J.; Whalen, G. Machine Learning of Clinical Performance in a Pancreatic Cancer Database. *Artif. Intell. Med.* **2010**, *49*, 187–195. [CrossRef] [PubMed]
26. Allyn, J.; Allou, N.; Augustin, P.; Philip, I.; Martinet, O.; Belghiti, M.; Provenchere, S.; Montravers, P.; Ferdynus, C. A Comparison of a Machine Learning Model with EuroSCORE II in Predicting Mortality after Elective Cardiac Surgery: A Decision Curve Analysis. *PLoS ONE* **2017**, *12*, e0169772. [CrossRef] [PubMed]
27. Arvind, V.; Kim, J.S.; Oermann, E.K.; Kaji, D.; Cho, S.K. Predicting Surgical Complications in Adult Patients Undergoing Anterior Cervical Discectomy and Fusion Using Machine Learning. *Neurospine* **2018**, *15*, 329–337. [CrossRef]
28. Qin, J.; Chen, L.; Liu, Y.; Liu, C.; Feng, C.; Chen, B. A Machine Learning Methodology for Diagnosing Chronic Kidney Disease. *IEEE Access* **2020**, *8*, 20991–21002. [CrossRef]
29. Geurts, P.; Ernst, D.; Wehenkel, L. Extremely Randomized Trees. *Mach. Learn.* **2006**, *63*, 3–42. [CrossRef]
30. Gotz, M.; Weber, C.; Blocher, J.; Stieltjes, B.; Meinzer, H.; Maier-Hein, K. Extremely Randomized Trees Based Brain Tumor Segmentation. *Proceeding BRATS Chall.-MICCAI* **2014**, *14*, 6–11.
31. Alawadi, S.; Mera, D.; Fernández-Delgado, M.; Alkhabbas, F.; Olsson, C.M.; Davidsson, P. A Comparison of Machine Learning Algorithms for Forecasting Indoor Temperature in Smart Buildings. *Energy Syst.* **2022**, *13*, 689–705. [CrossRef]
32. Damaševičius, R.; Venčkauskas, A.; Toldinas, J.; Grigaliūnas, Š. Ensemble-based Classification Using Neural Networks and Machine Learning Models for Windows Pe Malware Detection. *Electronics* **2021**, *10*, 485. [CrossRef]
33. Jun, Z.; Youqiang, Z.; Wei, C.; Fu, C. Research on Prediction of Contact Stress of Acetabular Lining Based on Principal Component Analysis and Support Vector Regression. *Biotechnol. Biotechnol. Equip.* **2021**, *35*, 462–468. [CrossRef]
34. Kruse, C.; Eiken, P.; Vestergaard, P. Machine Learning Principles Can Improve Hip Fracture Prediction. Calcif. *Tissue Int.* **2017**, *100*, 348–360. [CrossRef] [PubMed]
35. Chen, T.; Guestrin, C. XGBoost: A Scalable Tree Boosting System. In Proceedings of the the 22nd ACM SIGKDD International Conference on Knowledge Discovery and Data Mining, San Francisco, CA, USA, 13–17 August 2016; pp. 785–794. [CrossRef]
36. Breiman, L. Random Forests. *Mach. Learn.* **2001**, *45*, 5–32. [CrossRef]
37. Noble, W.S. What Is a Support Vector Machine? *Nat. Biotechnol.* **2006**, *24*, 1565–1567. [CrossRef] [PubMed]
38. Gao, S.; Li, H. Breast Cancer Diagnosis Based on Support Vector Machine. In Proceedings of the 2012 2nd International Conference on Uncertainty Reasoning and Knowledge Engineering, Jalarta, Indonesia, 14–15 August 2012; pp. 240–243. [CrossRef]
39. Lin, W.; Tian, X.; Lu, X.; Ma, D.; Wu, Y.; Hong, J.; Yan, R.; Feng, G.; Cheng, Z. Prediction of Bedridden Duration of Hospitalized Patients by Machine Learning Based on EMRS at Admission. *CIN Comput. Inform. Nurs.* **2022**, *40*, 251–257. [CrossRef] [PubMed]
40. Jin, R.; Chen, W.; Sudjianto, A. An Efficient Algorithm for Constructing Optimal Designs of Computer Experiments. *Int. Des. Eng. Tech. Conf. Comput. Inf. Eng. Conf.* **2003**, *37009*, 545–554.
41. Schwarzkopf, R.; Meftah, M.; Marwin, S.E.; Zabat, M.A.; Muir, J.M.; Lamb, I.R. The Use of Imageless Navigation to Quantify Cutting Error in Total Knee Arthroplasty. *Knee Surg. Relat. Res.* **2021**, *33*, 43. [CrossRef]
42. Sohail, M.; Park, J.; Kim, J.Y.; Kim, H.S.; Lee, J. Modified Whiteside's Line-Based Transepicondylar Axis for Imageless Total Knee Arthroplasty. *Mathematics* **2022**, *10*, 3670. [CrossRef]
43. Sershon, R.A.; Courtney, P.M.; Rosenthal, B.D.; Sporer, S.M.; Levine, B.R. Can Demographic Variables Accurately Predict Component Sizing in Primary Total Knee Arthroplasty? *J. Arthroplast.* **2017**, *32*, 3004–3008. [CrossRef]
44. Kang, K.T.; Koh, Y.G.; Son, J.; Kwon, O.R.; Lee, J.S.; Kwon, S.K. Influence of Increased Posterior Tibial Slope in Total Knee Arthroplasty on Knee Joint Biomechanics: A Computational Simulation Study. *J. Arthroplast.* **2018**, *33*, 572–579. [CrossRef]
45. Estupinan, J.A.; Bartel, D.L.; Wright, T.M. Residual Stresses in Ultra-High Molecular Weight Polyethylene Loaded Cyclically by a Rigid Moving Indenter in Nonconforming Geometries. *J. Orthop. Res.* **1998**, *16*, 80–88. [CrossRef] [PubMed]
46. Sathasivam, S.; Walker, P.S. A Computer Model with Surface Friction for the Prediction of Total Knee Kinematics. *J. Biomech.* **1997**, *30*, 177–184. [CrossRef] [PubMed]
47. Patil, N.A.; Njuguna, J.; Kandasubramanian, B. UHMWPE for Biomedical Applications: Performance and Functionalization. *Eur. Polym. J.* **2020**, *125*, 109529. [CrossRef]
48. Godest, A.C.; Beaugonin, M.; Haug, E.; Taylor, M.; Gregson, P.J. Simulation of a Knee Joint Replacement during a Gait Cycle Using Explicit Finite Element Analysis. *J. Biomech.* **2002**, *35*, 267–275. [CrossRef]
49. Knight, L.A.; Pal, S.; Coleman, J.C.; Bronson, F.; Haider, H.; Levine, D.L.; Taylor, M.; Rullkoetter, P.J. Comparison of Long-Term Numerical and Experimental Total Knee Replacement Wear during Simulated Gait Loading. *J. Biomech.* **2007**, *40*, 1550–1558. [CrossRef]
50. Innocenti, B.; Truyens, E.; Labey, L.; Wong, P.; Victor, J.; Bellemans, J. Can Medio-Lateral Baseplate Position and Load Sharing Induce Asymptomatic Local Bone Resorption of the Proximal Tibia? A Finite Element Study. *J. Orthop. Surg. Res.* **2009**, *4*, 26. [CrossRef]

51. Werner, F.W.; Ayers, D.C.; Maletsky, L.P.; Rullkoetter, P.J. The Effect of Valgus/Varus Malalignment on Load Distribution in Total Knee Replacements. *J. Biomech.* **2005**, *38*, 349–355. [CrossRef]
52. Morrison, J.B. The Mechanics of the Knee Joint in Relation to Normal Walking. *J. Biomech.* **1970**, *3*, 51–61. [CrossRef]
53. Kvålseth, T.O. Cautionary Note about R2. *Am. Stat.* **1985**, *39*, 279–285. [CrossRef]
54. Hodson, T.O. Root-Mean-Square Error (RMSE) or Mean Absolute Error (MAE): When to Use Them or Not. *Geosci. Model Dev.* **2022**, *15*, 5481–5487. [CrossRef]